International Journal of Refractory Metals and Hard Materials 128 (2025) 107029

Contents lists available at ScienceDirect

International Journal of Refractory Metals and Hard Materials

journal homepage: www.elsevier.com/locate/IJRMHM

Transition from 2D to 3D production of tantalum nitride by reactive powder bed fusion

A. Gatto [a], X. Zhu [a], P. Mengucci [b], S. Sabbatini [b], M.L. Gatto [c], M. Cabibbo [c], R. Groppo [d], S. Defanti [a,*], L. Denti [a]

[a] Università di Modena e Reggio Emilia, Dipartimento di Ingegneria "Enzo Ferrari", via P. Vivarelli, 10, 41125 Modena, Italy
[b] SIMAU, Università Politecnica delle Marche & UdR INSTM, via Brecce Bianche 12, 60131 Ancona, Italy
[c] Dipartimento di Ingegneria Industriale e Scienze Matematiche, Università Politecnica delle Marche, via Brecce Bianche 12, 60131 Ancona, Italy
[d] 3D4MEC S.r.l, Via Porrettana 48, 40037 Sasso Marconi, Bologna, Italy

ARTICLE INFO

Keywords:
Tantalum
Tantalum nitride
Additive manufacturing
Reactive powder bed fusion
Laser powder bed fusion
Bulk material

ABSTRACT

Tantalum nitride is an indispensable material for various technological applications due to its exceptional mechanical, thermal, electrical and biological properties. In the literature, tantalum nitride has so far mainly been produced in the form of thin coatings, which has limited its use in bulk shapes. This research represents a breakthrough advance in the simultaneous synthesis and consolidation of tantalum nitride and reports the successful fabrication of bulky shapes using laser powder bed fusion (LPBF) technology. The process involves the controlled interaction of tantalum powders with nitrogen within the LPBF chamber, resulting in the formation of tantalum nitride. The study demonstrates the feasibility of generating bulky tantalum nitride samples and opens up promising possibilities for practical applications in various industries such as implantology, electronics and solar water splitting. This innovative approach not only expands the application range of tantalum nitride, but also emphasizes the potential of additive manufacturing techniques in advancing materials synthesis and design.

1. Introduction

Tantalum nitride stands is an indispensable material in the field of advanced materials owing to its remarkable combination of properties such as a high melting point, excellent thermal stability, superior hardness and chemical inertness [1]. Shin et al. [2] reported several phases of tantalum nitride: equilibrium phases such as γ-Ta_2N hexagonal closed pack form, ε-TaN hexagonal and solid-solution of α-Ta(N) but also lots of metastable forms, including Ta_2N hexagonal, δ-TaN simple hexagonal, Ta_5N_6 hexagonal, Ta_4N_5 tetragonal, Ta_3N_5 orthorhombic. The allotropic configurations make tantalum nitride suitable for a variety of applications ranging from microelectronics to aerospace components.

One of the most common uses of tantalum nitride is in hard coatings [3], which are produced, for example, by physical vapour deposition [4]. Tantalum nitride is a refractory material with high corrosion and wear resistance and good mechanical properties [5,6]. In addition, TaN thin films also have excellent electrical properties, which enable their use in the manufacture of energy commutators, ignition transducers [7] and strain gauges [8]. Tantalum nitride can also be used for advanced, environmentally valuable applications. The current focus on pollution and energy scarcity is driving research in the field of photocatalytic materials. Photocatalytic materials are essential for water splitting and the degradation of pollutants. Tantalum nitride (Ta_3N_5) exhibits good photocatalytic activity [9], it has a broad wavelength absorption (from the UV range to at least 600 nm) and can theoretically achieve an efficiency of about 17 % in the conversion of solar energy into hydrogen [10].

Tantalum nitride has outstanding biomedical properties (corrosion resistance, chemical stability and histocompatibility) [11] and excellent blood compatibility, making it a potential replacement for low-temperature isotropic pyrolytic carbon in artificial heart valves [12]. Corona-Gomez et al. deposited tantalum nitride directly on biomedical grade CrCoMo alloy, and the coating showed high adhesion to the substrate. The coating also reduced the wear rate, resulting in a longer hip joint life [13]. Other authors used tantalum nitride coatings on titanium alloy implants to improve their biocompatibility (especially cell adhesion and proliferation) and bioactivity of osteogenesis [14]. Babaei et al. [15] deposited nanostructured TaN coatings using a reactive DC-

* Corresponding author.
E-mail address: silvio.defanti@unimore.it (S. Defanti).

https://doi.org/10.1016/j.ijrmhm.2024.107029
Received 22 July 2024; Received in revised form 13 December 2024; Accepted 18 December 2024
Available online 22 December 2024

magnetron sputtering and found that hexagonal and orthorhombic TaN phases lead to a denser microstructure and better corrosion behavior.

Finally, the low temperature coefficient of resistivity, the low voltage coefficient of resistivity and the good barrier properties in copper compounds are suitable for use in the semiconductor industry [16]. The barrier effect is strongly dependent on the phases present in the nitride. In fact, the behavior of the nitride can change considerably with the same chemical composition [17]. The phase stability of 1:1 tantalum nitride has been studied in an interesting way by Grumski et al. [18].

Despite its numerous advantages, the practical use of tantalum nitride is mainly limited to thin-film coatings due to the difficulties in producing bulk material. In the production of thin films, the choice of process parameters can have a significant impact not only on the macroscopic quality of the film, but above all on its structural properties. Several authors observed the contemporary production of different tantalum nitride phases by DC magnetron sputtering systems as a function of the N_2/Ar gas ratio [17,19]. The nitrogen flow in the magnetron sputtering system influences the phase formation of tantalum nitride and consequently its hardness, wear, adhesion, corrosion resistance, and biocompatibility [20,21]. Ramezani et al. observed the effects of nitrogen ion flux on tantalum nitride films prepared by nitrogen ion implantation [22]. Other authors used direct current sputtering to produce tantalum nitride and correlated the resistivity of tantalum nitride with structural properties [23,24]. Lei et al. used the concentration of the reactive gas NH_3 to obtain a single-phase TaN_2 [25]. X. Zhao et al. demonstrated the production of an atomic layer of tantalum nitride by CVD using a suitable precursor [26]. The atomic layer deposition of tantalum nitride is carried out with the plasma-assisted solution [27], which allows a wide range of chemical precursors and a process at low temperatures. An inductively coupled plasma-assisted sputtering system guarantees control over the crystal structure of the film and increases the density of the layer [28].Baik et al. investigated the production of tantalum nitride by inductively coupled plasma-assisted sputtering [29]. Hee et al. produced a bioactive tantalum nitride coating by cathodic vacuum arc deposition [30].

Conventional manufacturing methods have often struggled to achieve the synthesis of bulky tantalum nitride, limiting its potential in various industrial sectors. Recently, some authors have hypothesized that light absorbers can be produced using metamaterials. The artificial structures (which do not occur in nature) of metamaterials offer original interactions with light. Lu et al. [31] see additive manufacturing (AM) as a promising solution for the fabrication of broadband metamaterials as adsorber metamaterials, but claim that tantalum nitride is not suitable for fabrication using additive technology.

The advent of AM technologies has revolutionised the landscape of material synthesis, offering unprecedented opportunities for the production of complex geometries and customised components. Among the myriad AM techniques, Laser Powder Bed Fusion (LPBF) has emerged as a frontrunner due to its high precision, versatility and ability to process a wide range of materials such as metals, ceramics and composites. Recent developments include the use of a reactive atmosphere in the build chamber to achieve in-situ synthesis of specific phases or reinforced microstructures [32,33]. The present research leverages the unique properties of reactive LPBF to explore a novel approach for the synthesis and fabrication of TaN in bulky forms. The motivation for this research endeavor stems from the critical need to expand the application range of tantalum nitride beyond conventional thin film coatings. Whilst thin films are widely used in microelectronics, corrosion protection and wear resistant coatings, the limitations associated with film thickness and substrate compatibility have hindered the wider application of TaN in various engineering domains. By moving from coatings to bulky shapes, this study aims to unlock new opportunities for the use of tantalum nitride in areas such as aerospace, automotive, energy storage and biomedical engineering.

Table 1
Composition of the raw powder as provided by the manufacturer. Values are in wt%.

Ta	O	H	N	C	Cr	Fe	Ni
99.99	0.028	0.005	0.003	<0.005	<0.001	<0.001	<0.001

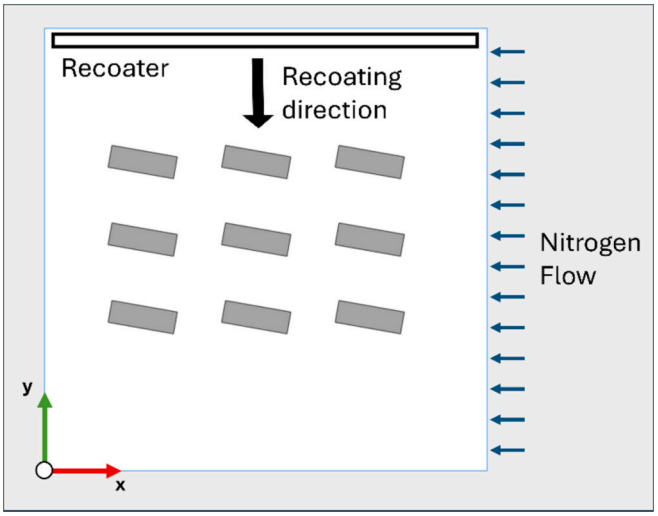

Fig. 1. Layout of the build job with the nitrogen flow and recoating direction.

2. Experimental procedures

2.1. L-PBF specimens manufacturing

Tekna (Mâcon, France) supplied gas atomized pure tantalum powder with the nominal chemical composition shown in Table 1, and the particle size distribution $D_{10} = 19$ μm and $D_{99} = 45$ μm, as reported in the manufacturer datasheet.

The powder was used to produce solid specimens using a 3D4steel LPBF machine (3D4MEC S.r.l., Sasso Marconi, Bologna, Italy) equipped with a 500 W Raycus Yb fiber CW laser (Wuhan Raycus Fiber Laser Technologies Co., Wuhan, Hubei, China) operating in a nitrogen atmosphere, with a wavelength ranging from 1050 to 1090 nm. The machine was equipped with an Intelli*SCAN* III 20 (SCANLAB GmbH, Puchheim, Germany) galvanometer head operating with a protective glass filter at an optimum wavelength of 1064 nm. Nitrogen was generated by a local generator (Barzagli Generatori S.a.s, Grosseto, Italy) with a purity of 99.9 % and flooded into the build chamber. The machine was equipped with a Minox i 200 (Ntron Ltd., Navan, Ireland) oximeter, which measures the percentage of oxygen in the working chamber and eventually stops production if the oxygen level exceeds 1 %. The measured percentage of oxygen in the working chamber was <0.7 % throughout the production.

Specimens of $15 \times 5 \times 5$ mm^3 (x, y, z) were built on a steel base plate (C40 steel) after 5 layers of support structures to facilitate the removal of the samples. The supports used are of the volumetric type, with a rhomboid mesh structure, a cell size of (1.5×1.5) mm^2, and a single section size of 0.6 mm. The scanning strategy used for the specimens was a standard hatching, where the order of consolidation was outer contour, inner contour and then infill. The scan direction of the infill of the first layer was inclined by 22.5° with respect to the N_2 flow direction, while the scan vector rotation was set to 67° for the subsequent layers. The direction of the recoater was perpendicular to the N_2 flow direction, while the samples were placed on the buildplate at an angle of 10° to the direction of the recoater. Fig. 1 shows the geometry of the samples and the layout of the job.

The various sets of process parameters used to manufacture the

Table 2
Process parameters used for specimens production: P – laser power, v – laser scanning speed, h - hatch distance, t - layer thickness and E_s - surface energy density.

Sample ID [P_v_E_s]	P [W]	V [mm/s]	h [mm]	t [mm]	E_s [J/mm^2]
150_90_12	150	90	0.14	0.05	12
150_120_9	150	120	0.14	0.05	9
150_150_7	150	150	0.14	0.05	7

specimens are listed in Table 2. This results in a surface energy density E_s, which is calculated as $E_s = P / (v \bullet h)$ where P is the laser power, v is the laser scanning speed and h is the hatch distance.

2.2. Density analysis

After production, the specimens were subjected to density measurement according to the ASTM B962–23 standard [34] using an Ohaus PA214C analytical balance (Ohaus, Nänikon, Switzerland) equipped with an Archimedes density kit. The measurement procedure was

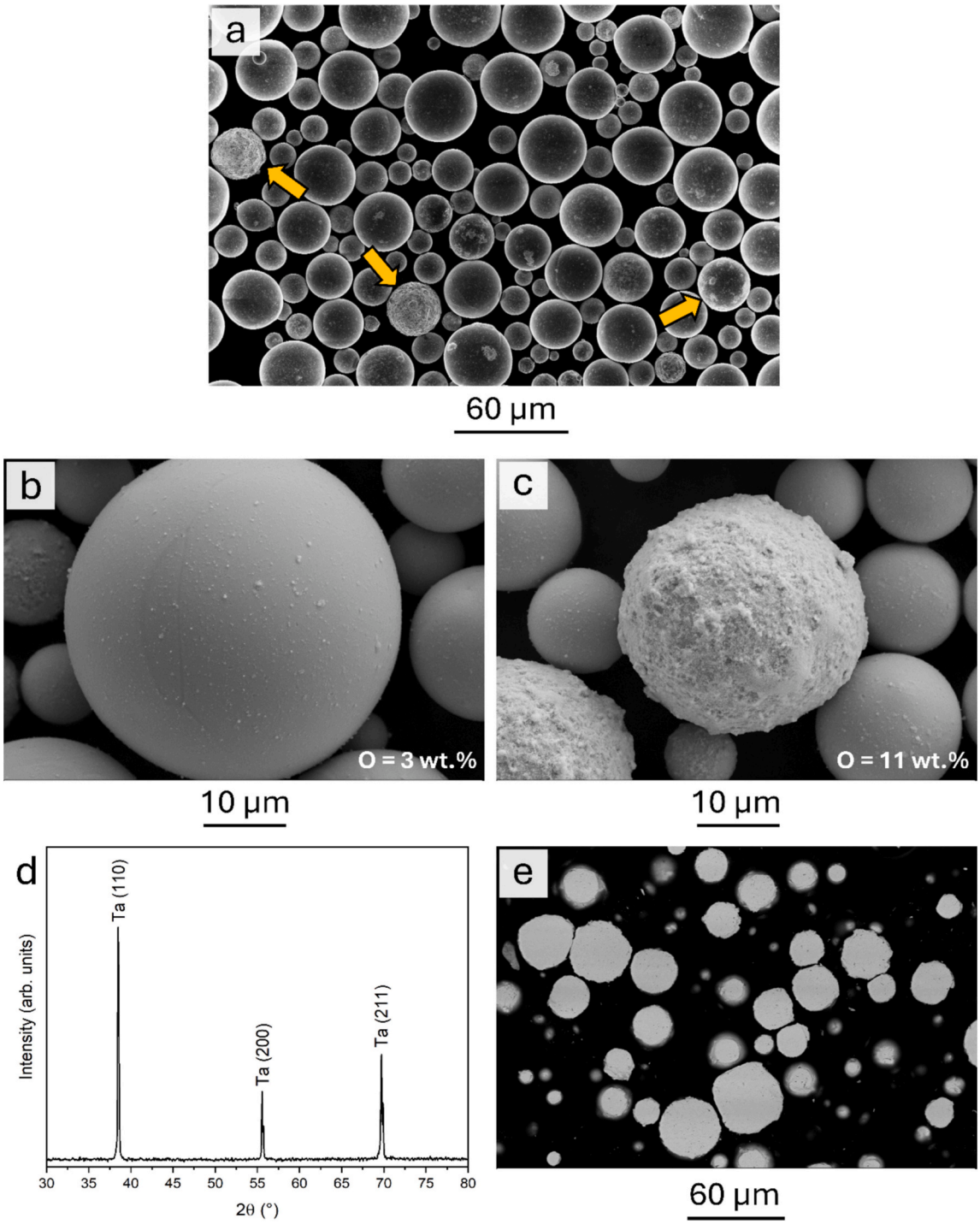

Fig. 2. FESEM images of the raw powder obtained by the in-lens detector of the FESEM microscope. (a) Overall image, arrows indicate particles with rough surface; (b) SE detector, particle with smooth surface and (c) SE detector, particle with rough surface. The oxygen content was obtained by EDS analysis in "spot mode". (d) XRD pattern of the raw powder (e) Sectioned powder particles.

repeated three times for each sample.

2.3. Structural characterization

The raw powder and all the produced specimens were subjected to structural characterization by scanning electron microscopy (SEM), energy dispersive spectroscopy (EDS), X-ray diffraction (XRD) and Fourier transform infrared spectroscopy (FTIR).

The morphology and chemical composition of the samples were investigated by a Zeiss Supra 40 high-resolution field emission scanning electron microscope (FESEM) equipped with a Bruker Quanta 200 microanalyser (EDS). EDS analyses were performed both in "area mode", i.e. over the entire scanned field of view, and in "spot mode" with a stationary electron beam to obtain the chemical composition of the sample from an area as large as the spot of the electron beam. Properly prepared samples viewed in cross section were analyzed in EDS "line scan" mode to detect elemental variations from surface to bulk.

For the FESEM/EDS analysis, the raw powder was dispersed on a carbon disc glued to the top of an aluminum stub. To investigate the internal structure of the particles, the raw powder was embedded in HARDROCK 554 epoxy resin, ground by emery paper and polished with diamond paste.

The XRD investigations were carried out using a Bruker D8 Advance diffractometer operating at $V = 40$ kV and $I = 40$ mA, with Cu-Kα radiation, in the angular range $2\theta = 5°$- $80°$. The XRD patterns were analyzed using the DIFFRAC.EVA software package including ICDD—PDF 2 for search/match analysis. The shape analysis of the XRD peaks was performed with the OriginPro 2024 software package. Rietveld analysis of the XRD patterns performed using the MAUD software [35] allowed quantitative information on the total amount of phases present in the samples to be obtained.

FTIR analysis was carried out using a Perkin Elmer Spectrum GX1 spectrometer with the ATR accessory and a ZnSe crystal on the samples reported in Table 2. The spectra were recorded in the 4000–500 cm^{-1} range with a resolution of 4 cm^{-1}. Each spectrum was the average of 32 scans. The samples were placed directly on the ZnSe crystal without any preparation. Three IR spectra were recorded for each sample and the average absorbance spectrum was calculated. The background spectrum was obtained from the clean crystal before each measurement. The raw IR spectra were then converted to absorbance mode and vector normalized using Perkin-Elmer's Spectrum 10.4.0 software from.

The sample built in the condition 150_150_7 was subjected to further analyses as it was considered the most promising due to its consolidation behavior. Three different specimens with the 150_150_7 setup were prepared to analyze (a) the upskin surface, (b) the rupture surface and (c) the internal microstructure. Micro- and nano-hardness tests were performed on this last sample.

The upskin surface was prepared by placing it on a stab in its as-built condition. In addition, a fracture surface was obtained by manually fracturing an as-built sample and analyzing a surface parallel to the build direction (*Z*-axis).

For the microstructure analyses, a 150_150_7 sample was sectioned and embedded in low shrinkage Technovit 4000 resin. After resin consolidation, the sample was ground and finally vibro-polished with a suspension of silica particles with a size of 0.05 um. The sample was then chemically etched with a solution of 15 mL sulphuric acid, 5 mL nitric acid and 5 mL hydrofluoric acid [36] for a total of 2 s. Then, the microstructure was observed using a Nova NanoSEM 450 scanning electron microscope.

2.4. Micro-hardness and nano-hardness analysis

Vickers micro-hardness measurements, according to the UNI EN ISO 6507-1 standard [37] were carried out using a Remet HX-1000 (Remet,

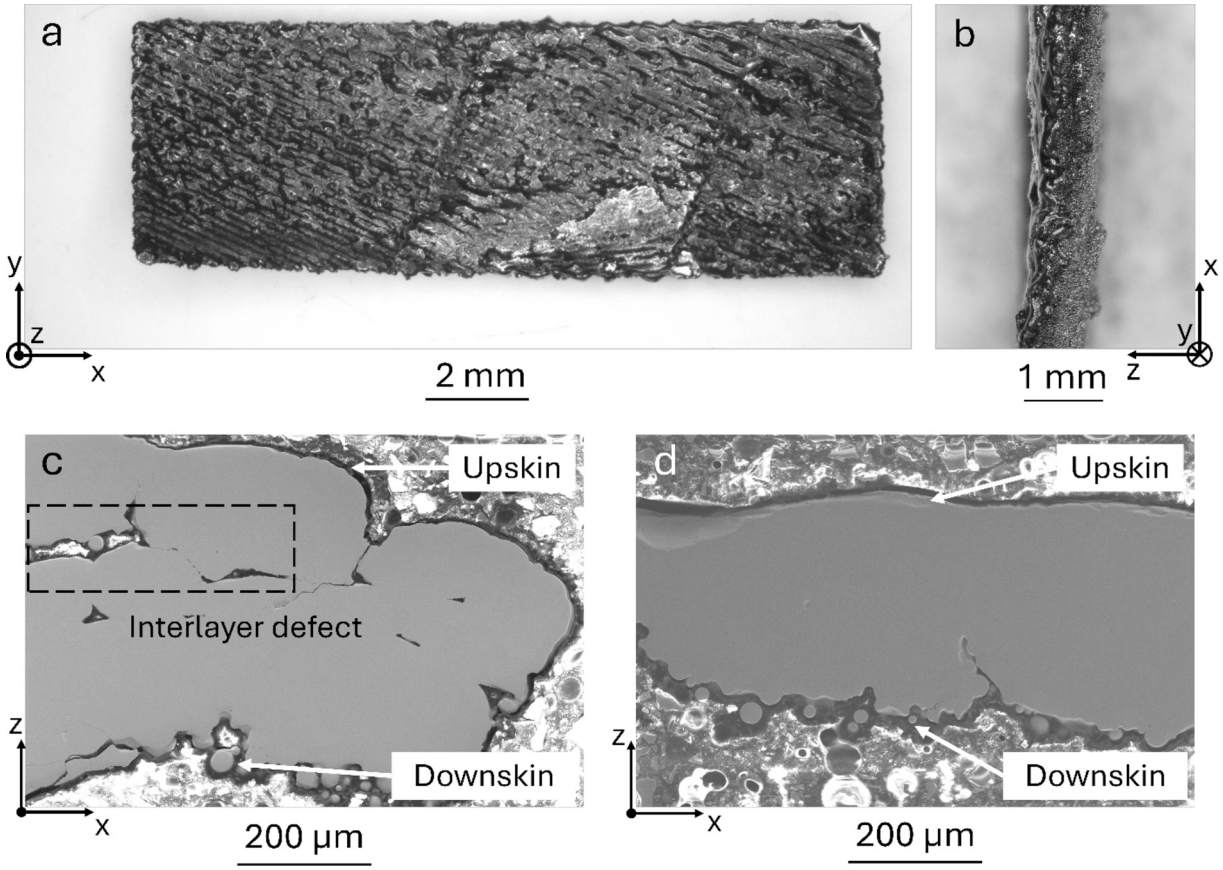

Fig. 3. Images of 150_150_7 solid sample: (a) overall upskin view, (b) detailed view along the thickness of the sample, (c-d) SEM images of a polished section.

Bologna, Italy) microdurometer. The tests were performed with a load of 0.1 kgf (HV 0.1) and a dwell time of 10 s on the polished section of the sample used for the microstructural observations and obtained using the procedure described in section 2.3. Ten indentations were made randomly in the center of the specimen thickness and distributed along its entire length.

Instrumented indentation tests were performed in an area of the same sample where the consolidation was effective, far from inter-layer defects, according to the guidelines of the ISO 14577-1 standard [38] in the nano range, using an Anton Paar NHT3 (Anton Paar, Graz, Austria). The instrument consists of a vibration damping stage, a microscope, and an indenter with a Berkovich tip. The indentation cycle was set with a force application time of 30 s, a dwell time of 10 s and a force removal time of 30 s. The Oliver & Pharr method was used to calculate the hardness. Five force levels were defined to test the sensitivity of the material to the applied force: 50, 100, 150, 200, 250 mN. For each level, 5 indentations were made. The values of indentation hardness (HIT), Vickers hardness (HVIT) and indentation modulus (EIT) were calculated for each force level.

3. Results and discussion

3.1. Powder characterization

The raw powder observed by the in-lens detector of the FESEM microscope consists of spherical particles with a size in the range of 5–40 μm, as shown in Fig. 2(a). Statistical analysis of the FESEM images using the ImageJ software confirmed the particle size distribution as specified by the manufacturer. Fig. 2(a) shows that although most of the particles have a smooth surface, some show a rough surface (indicated by arrows in Fig. 2(a)). The FESEM observations carried out with the SE (Secondary Electron) detector made it possible to evidence differences in the surface morphology of the particles (Fig. 2(b-c)). Fig. 2(b) shows the smooth surface of a particle, while Fig. 2(c) shows a detail of the morphology of a rough particle. The EDS analysis, which was performed in "spot mode" on both particles, resulted in a high oxygen content in the particle with the rough surface. The percentage values are shown in Fig. 2(b-c).

The XRD pattern of the raw powder is shown in Fig. 2(d). The diffraction peaks are due to the only phase present in the sample, namely α-Ta, body centered cubic (bcc), space group Im-3 m (229), and nominal lattice parameter a = 0.330580 nm (ICDD-PDF2 file n. 4–788). The width and intensity of peaks indicate a well crystallized Ta phase. No other crystalline compounds are present in the raw powder. However, the presence of oxygen detected by EDS analysis suggests the possible formation of tantalum oxide. Therefore, the absence of peaks attributable to tantalum oxide in the XRD pattern in Fig. 2(d) can be ascribed to the formation of a thin and amorphous surface oxide layer coating the particles of the raw powder.

The SEM image of the inner structure of the powder particles is shown in Fig. 2(e). In the particles, some pores are dispersed in a general compact structure. The presence of pores, which form during the cooling phase of the gas atomization process used to produce the raw powder, reduces the density of the material. The manufacturer's datasheet gives 10.6 g/mm^3 as the value for the tap density of the powder, measured according to ASTM-B527 method. The nominal value of the α-Ta bulk density is 16.637 g/cm^3, as stated in ICDD file No. 4–788.

3.2. L-PBF specimens characterization

During the L-PBF process, all the specimens (150_90_12, 150_120_9, and 150_150_7, as indicated in Table 2) warped and rose above the powder bed after 5–10 layers, leading to the job abortion. This is likely due to excessive shrinkage-induced stresses and an indication that the process parameters need to be further optimized. However, for the samples produced with the lowest energy density (150_150_7), the build proceeded successfully for a higher number of layers than at the more energetic conditions. The largest sample that could be built (Fig. 3(a-b)) has a size of 15 × 5 mm^2 (x, y), with a maximum thickness of 300–400 μm (z), even though there are clear signs of adhesion problems between the layers. Inter-layer defects can be better observed on the polished section of a 150_150_7 specimen (Fig. 3(c-d)).

Poor adhesion between the layers is also a possible symptom of insufficient remelting due to lack of energy. These results suggest that a higher energy density is required to achieve a deeper melt pool and better bond between the layers. However, more energetic parameters would increase the risk of warping and job failure. It can be assumed that a tighter attachment of the part to the build plate must be ensured before attempting to optimize the parameters of the laser process towards better control of cooling rates and the shape of the melt pool. Nevertheless, the result is already the first proof of the feasibility of bulk consolidation of tantalum nitride.

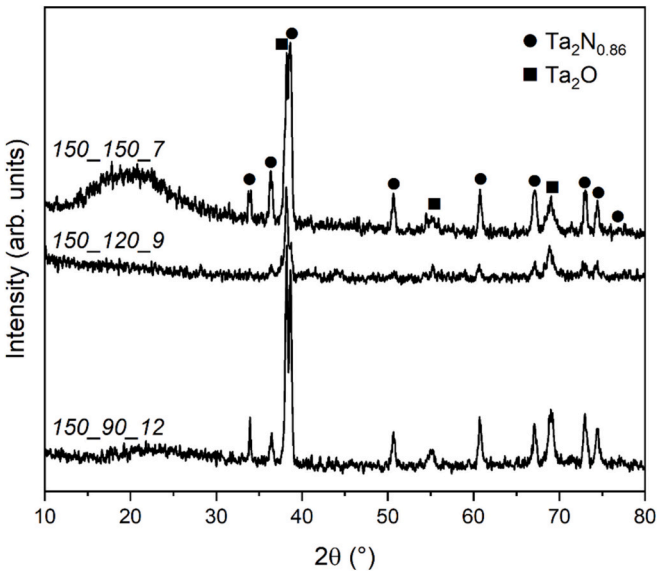

Fig. 4. XRD patterns of samples manufactured with the optimized printing parameters.
Full dot – $Ta_2N_{0.86}$; full square - Ta_2O.

Table 3
Quantitative composition of samples as provided by the Rietveld refinement.

Sample name	$Ta_2N_{0.86}$ (wt%)	Ta_2O (wt%)
150_150_7	77	23
150_120_9	54	46
150_90_12	74	26

3.2.1. Structural characterization

The XRD patterns of the samples manufactured with the optimized printing parameters listed in Table 2 are reported in Fig. 4.

XRD patterns in Fig. 4 show peaks of β-$Ta_2N_{0.86}$, hexagonal, space group P-31 m (162), nominal lattice parameters a = 0.5285 nm and c = 0.4919 nm (ICDD-PDF2 file n. 89–5199) and of Ta_2O, cubic, space group I23 (197), nominal lattice parameter a = 0.668 nm (ICDD-PDF2 file n. 74–2305). No peaks of pure Ta were detected by the XRD analysis. Peak shape analysis and Rietveld refinement of the XRD patterns allowed obtaining the relative amount of phases present in the samples. The results are reported in Table 3.

Sample 150_150_7 produced with the lowest value of surface energy density (E_{surf} = 7 J/mm^2) contains the highest amount of tantalum nitride ($Ta_2N_{0.86}$) compared to all other samples. In addition to the

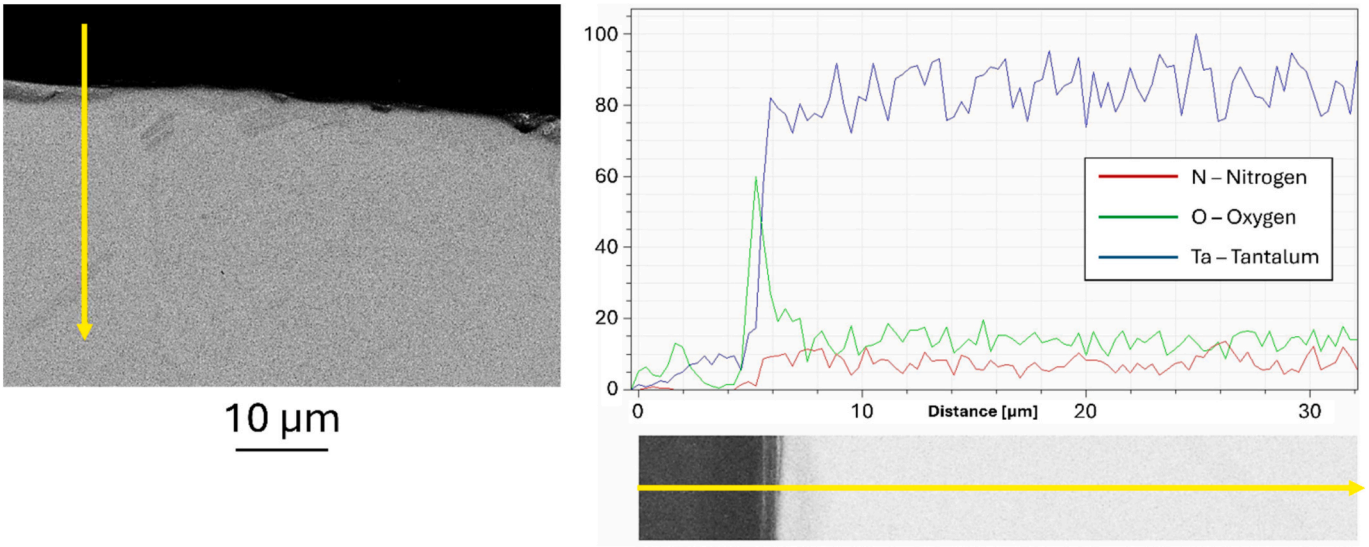

Fig. 5. EDS analysis in line scan mode through the surface of the 150_150_7 specimen observed in cross section. Blue line – Ta, green line – O, red line – N. (For interpretation of the references to colour in this figure legend, the reader is referred to the web version of this article.)

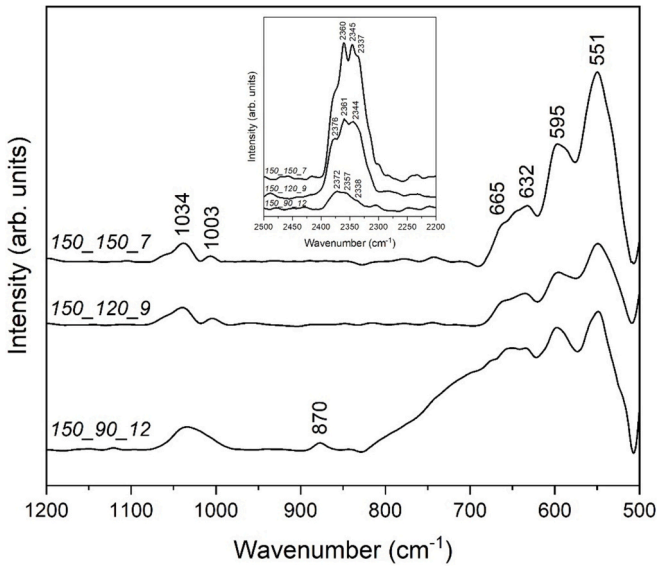

Fig. 6. FTIR spectra of samples. The inset shows the wavenumber range 2500–2000 cm^{-1}.

nitride, this sample also exhibits peaks that can be attributed to the tantalum oxide Ta_2O (Fig. 4). All the compounds present in sample 150_150_7 ($Ta_2N_{0.86}$ and Ta_2O) are well crystallized, as evidenced by the narrow width of the peaks (Fig. 4). However, the XRD pattern of sample 150_150_7 also shows a broad diffraction effect at about $2\theta = 20°$, which suggests the presence of amorphous and/or poorly crystallized compounds. The formation of poorly crystallized compounds in this sample is a direct result of the high cooling rates typical of the LPBF process and the low energy density of this sample, which limits the thickness of the remelted layer during laser exposure.

The sample produced with E_{surf} = 9 J/mm^2 (150_120_9) has the highest proportion of tantalum oxide (Table 3). On the contrary, at the highest value of the surface energy density (E_{surf} = 12 J/mm^2), the amount of tantalum nitride prevails over the oxide and all compounds are well crystallized (Fig. 4 and Table 3). However, a broad diffraction effect of very low intensity around $2\theta = 20°$ is also visible in this sample, indicating the formation of amorphous and/or poorly crystallized compounds, albeit in smaller quantities than in sample 150_150_7.

The EDS analysis carried out in area mode evidenced the presence of nitrogen in all samples. The total amount of nitrogen is almost the same, about 1 wt%, regardless of the manufacturing conditions.

The EDS analysis in line scan mode was carried out on samples that were properly prepared and observed in cross-section. The results of these analyses, shown in Fig. 5 for sample 150_150_7, are representative of all samples analyzed.

When the sample is line-scanned from regions outside the surface to about 30 µm inside, the signals of all elements undergo an abrupt change at the sample surface. The change is most evident in the oxygen signal (green line), which has the highest concentration at the sample surface, indicating the presence of a surface oxide layer. Inside the sample, the oxygen remains almost constant with an average value of about 15 wt%. Nitrogen (red line) is not present outside the sample, but is clearly present inside the sample with an almost constant concentration of about 1 wt%. The concentration of tantalum (blue line) remains almost constant throughout the sample. These results in combination with those of the XRD analysis indicate that the sample consists of a superficial Ta_2O layer, only a few micrometers thick, while the tantalum nitride $Ta_2N_{0.86}$ is present throughout the sample (Fig. 5).

FTIR analysis was used to examine the compounds formed in the samples and to understand the chemical bonding. The results of the FTIR analysis carried out on the manufactured samples are reported in Fig. 6. To facilitate comparison, the FTIR spectra in Fig. 6 have been shifted vertically.

In the spectral range between 500 and 700 cm^{-1}, the average spectra of the three samples analyzed show intense bands at 551, 595, and 632 cm^{-1}, confirming the presence of tantalum oxide, as they are representative of the Ta—O bond. In contrast, the region between 800 and 1000 cm^{-1}, shows less intense bands, which originate from the stretching of the Ta—N bond and confirm the presence of tantalum nitride [10]. As described in the literature, the small peak at 870 cm^{-1} in the sample 150_90_12 can probably be assigned to the stretching mode of the Ta-O-Ta bonds [39].

The spectral range 2200–2600 cm^{-1}, is known to show the characteristic bands of the Ta═O double bond in Ta_2O_5. In particular, the band at 2335 cm^{-1} is attributed to the amorphous conformation of the tantalum oxide, obtained with annealing up to 500–600 °C, while the band at 2340 cm^{-1} is associated with the crystalline conformation of the metal oxide, obtained with annealing above 700 °C [39]. The spectra of samples 150_150_7 and 150_90_12 show bands representative of both

Table 4
Results of density measurements. Mean value and deviation of 3 measures are given.

Sample name	Density [g/cm^3]
150_90_12	15.5 ± 0.3
150_120_9	14.6 ± 0.7
150_150_7	15.4 ± 0.3

conformations (at 2337, 2345, and 2360 cm^{-1} and at 2338, 2357, and 2372 cm^{-1}, respectively), with a predominance of the crystalline phase, while the spectrum of sample 150_120_9 shows the bands at 2344, 2361, and 2376 cm^{-1}, confirming the presence of the only crystalline phase. These results are in close agreement with those obtained by the XRD analysis.

Overall, the spectral analysis of the three samples confirms the presence of both tantalum oxide and tantalum nitride. The different conformation of the latter in sample 150_90_12 and the presence of both an amorphous and a crystalline conformation of tantalum oxide in samples 150_150_7 and 150_90_12 indicate a strong influence of the value of the surface energy density. Further investigation and characterization of these samples could provide valuable insights into their properties and potential applications in various fields.

3.2.2. Density analysis

The results of the density measurement carried out on all samples are listed in Table 4. Within the uncertainties, the density values are similar for all samples.

The values obtained lie between the density of pure tantalum (16.7 g/cm^3 [40]) and tantalum nitride (13.7 g/cm^3 [40]). However, it is important to mention that this result could be influenced by the presence of closed pores in lack-of-fusion areas or at the interface between the layers.

As previously mentioned, samples 150_150_7 were subjected to a deeper characterization due to the better result in terms of the size of the consolidated parts compared to the other samples.

3.2.3. Upskin surface characterization

SEM observations of the top surface of the 150_ 150_7 sample are shown in Fig. 7(a-b). The images show very good surface integrity of the individual melt tracks, as well as good adhesion between neighboring tracks (Fig. 7(a-b)). The result indicates a good tuning of the LPBF parameters [41]. In addition, Fig. 7(b) reveals the presence of at least two phases, that continue through adjacent scan tracks.

3.2.4. Rupture surface characterization

Fig. 7(c-d) shows an overall view of the rupture surface of a

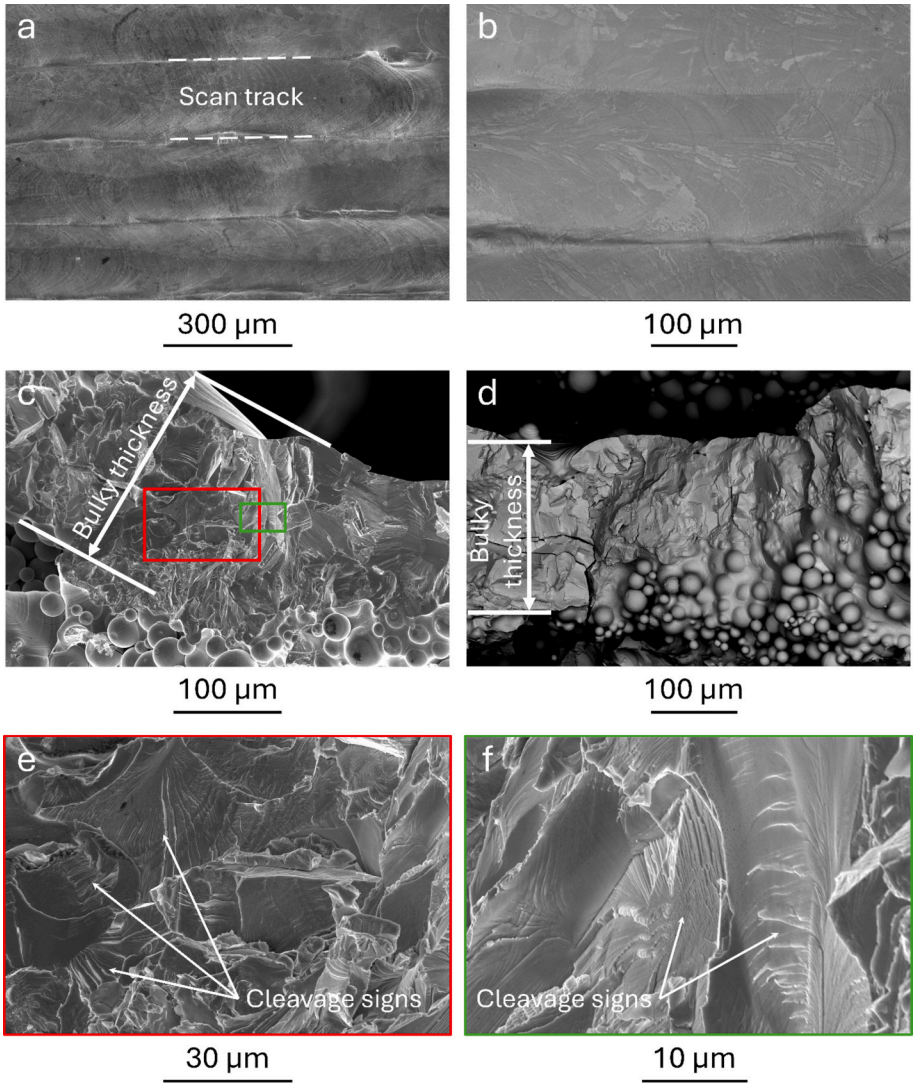

Fig. 7. SEM images of the specimen 150_150_7: (a) upskin surface, SE, 4 adjacent scan tracks (b) upskin surface, BSE, detail of scan tracks adhesion. (c) rupture surface, SE, overall view, (d) rupture surface, BSE, overall view, (e) and (f) detail of the cleavage phenomenon on the rupture surface.

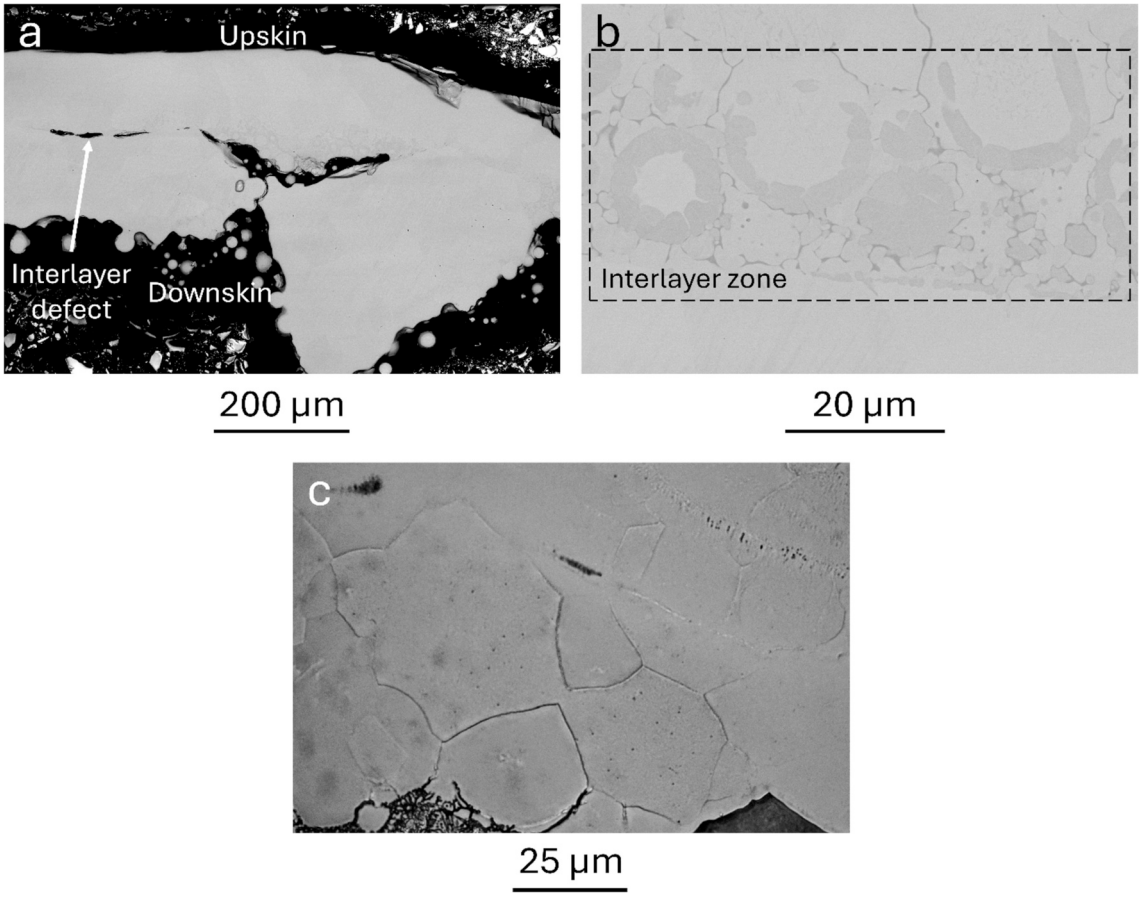

Fig. 8. Images of the section of specimen 150_150_7: (a) SEM image, BSE, overall view, (b) SEM image, BSE, detail of an insufficiently melted area (c) OM image of the etched surface;

150_150_7 sample that was manually fractured. The section shows a thickness of approx. 100–300 µm of bulky material, which has completely melted and become a solid part. Below the sample, the downskin region is visible, which consists of sintered and partially melted powder particles. The failure mechanism is fragile and is characterized by many cracks and frequent occurrence of the cleavage phenomenon (Fig. 7(e-f)).

3.2.5. *Microstructural characterization*

Fig. 8(a) shows an SEM image of a polished section of sample 150_150_7, which again demonstrates that the build-up has occurred to a local thickness of 0.6 mm, with interlayer detachment being the limiting factor in building higher parts. Fig. 8(b) shows that even where the sample is macroscopically solid, the interlayer zone suffers from incomplete melting as the original powder particles can still be recognised. After chemical etching, the samples exhibit a microstructure with predominantly equiaxed grains, as shown in Fig. 8(c). The observed microstructure is consistent with the microstructure of tantalum and tantalum oxide described in the literature [42]. In addition, the grains shown in Fig. 8(c) reflect the fracture surface shown in Fig. 7(e).

3.2.6. *Micro-hardness and nano-hardness analysis*

Hardness tests were performed on a section of sample 150_150_7 to test the material properties in a core area that should better represent the properties of the bulk material. The microhardness tests yielded a value of 862 ± 111 HV0.1, a value at the lower limit of the range measured by Kim and Cha [17] on thin TaN films deposited by D.C. magnetron sputtering at various N2/Ar gas ratios. Therefore, a more localised evaluation is performed by instrumented indentations, the results of which are shown in Table 5 for force levels of 50, 100 and 150 mN. The measurements at 200 and 250 mN are not shown as the depth of the indentation was outside the calibrated range of the instrument, resulting in an unreliable measurement. The hardness values determined with the load range of 50–150 mN show only very small deviations and no load dependence. In addition, the values are within the hardness range of 16 to 20 GPa specified by Bernoulli et al. [19] for a tantalum nitride film, while Leng et al. [43] measured higher values for Ta_2N. Details of the force-depth curves and of the indentations shape are given in Fig. 9(a-b).

Table 5
Results of indentations performed with three different force levels.

Force [mN]	EIT [GPa]		HIT [GPa]		HVIT [Vickers]	
	Mean	Std. Dev.	Mean	Std. Dev.	Mean	Std. Dev.
50	210	9	16.7	0.9	1540	85
100	210	7	16.0	0.4	1475	40
150	211	8	16.8	0.9	1555	80

4. Conclusions

This research represents a pioneering breakthrough in the synthesis and construction of tantalum nitride and marks the first successful fabrication of bulky TaN shapes utilizing the reactive LPBF technique. By harnessing the intrinsic reactivity of tantalum with nitrogen under specific processing conditions, the research has achieved unprecedented success in the consolidation of samples consisting of tantalum nitride and oxide. The presence of oxide is not ascribed to the manufacturing phase itself, but to the original supply conditions of the powder.

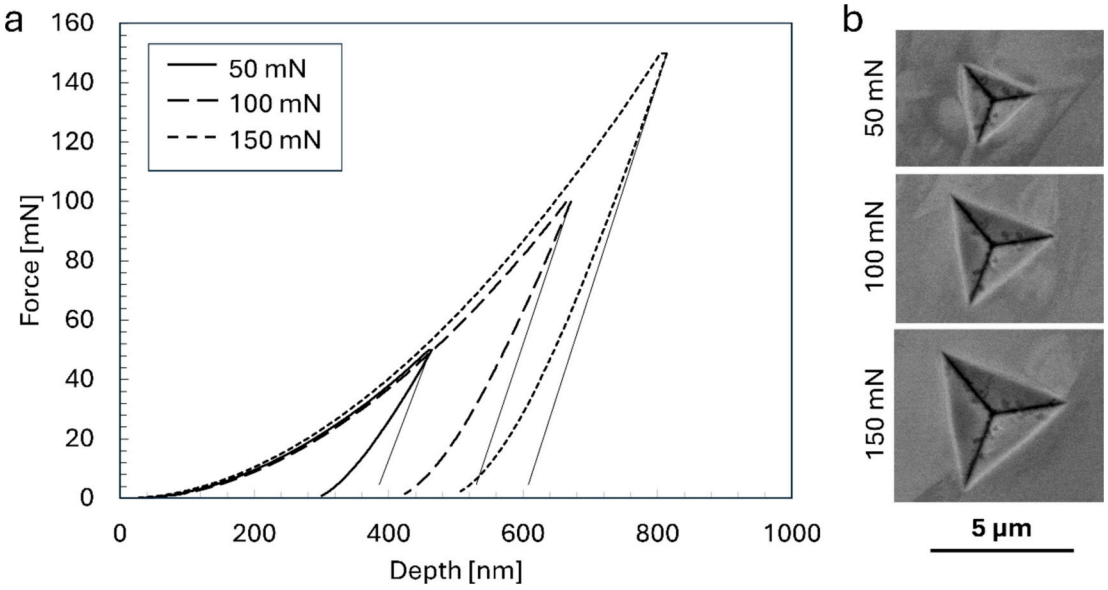

Fig. 9. (a) Force vs. depth plot of representative indentations for the 3 force levels and (b) backscattered electron images of the indentations.

The presence of TaN was confirmed by XRD analysis, which detected $Ta_2N_{0.86}$, FTIR analysis, which identified Ta—N bonds, and hardness test results, which were consistent with values reported in the literature for TaN. Additionally, EDS analysis confirmed the presence of nitrogen in the sample, further supporting the formation of TaN.

Further studies are required to optimize the process parameters and enable the production of larger components. However, the results not only open up the possibility of customising TaN for specific applications, but also underline the transformative potential of additive manufacturing for progress in materials science and engineering.

Ethical approval

Not applicable.

Funding

The authors received no financial support.

CRediT authorship contribution statement

A. Gatto: Supervision, Project administration, Conceptualization. **X. Zhu:** Visualization, Methodology, Investigation. **P. Mengucci:** Writing – original draft, Project administration, Investigation. **S. Sabbatini:** Writing – original draft, Investigation. **M.L. Gatto:** Writing – original draft, Data curation. **M. Cabibbo:** Supervision. **R. Groppo:** Writing – original draft, Resources, Investigation. **S. Defanti:** Writing – review & editing, Writing – original draft, Investigation. **L. Denti:** Writing – review & editing, Validation.

Declaration of competing interest

The authors declare that they have no known competing financial interests or personal relationships that could have appeared to influence the work reported in this paper.

Data availability

Research data is available on request.

References

[1] A. Fattah-alhosseini, M. Pourmahmoud, Passive and semiconducting properties assessment of commercially pure tantalum in Hank's physiological solution, J. Mater. Eng. Perform. 27 (1) (Jan. 2018) 116–123, https://doi.org/10.1007/s11665-017-3108-6.

[2] C.-S. Shin, Y.-W. Kim, D. Gall, J.E. Greene, I. Petrov, Phase composition and microstructure of polycrystalline and epitaxial TaNx layers grown on oxidized Si (001) and MgO(001) by reactive magnetron sputter deposition, Thin Solid Films 402 (1–2) (Jan. 2002) 172–182, https://doi.org/10.1016/S0040-6090(01)01618-2.

[3] V. Singh, R.K. Sharma, R. Sehgal, An experimental investigation on nanomechanical and nanotribological behavior of tantalum nitride coating deposited on Ti6Al7Nb alloy, Tribol. Int. 194 (Jun. 2024) 109461, https://doi.org/10.1016/j.triboint.2024.109461.

[4] K.K. Amirtharaj Mosas, D.K. Devarajan, S. Hazra, G.S. Kaliaraj, Recent Advancements in Wear-Resistant Coatings Prepared by PVD Methods, 2022, pp. 174–195, https://doi.org/10.4018/978-1-7998-9683-8.ch008.

[5] K. Babaei, A. Fattah-alhosseini, H. Elmkhah, H. Ghomi, Surface characterization and electrochemical properties of tantalum nitride (TaN) nanostructured coatings produced by reactive DC magnetron sputtering, Surf. Interf. 21 (Dec. 2020) 100685, https://doi.org/10.1016/j.surfin.2020.100685.

[6] S. Padervand, M. Amiri, M. Mousavi Khoei, Optimization of electrolyte concentration for surface modification of tantalum using plasma electrolytic nitridation, Int. J. Refract. Met. Hard Mater. 87 (Feb. 2020) 105146, https://doi.org/10.1016/j.ijrmhm.2019.105146.

[7] X. Ren, Study on the ignition performance of TaN transducer by heat treatment, CONVERTER (Jul. 2021) 347–353, https://doi.org/10.17762/converter.67.

[8] L. Cao, Y. Wang, X. Sun, J. Zhou, L. Kang, N. An, Study on the fabrication and characteristics of tantalum-nitride (TaN) thin-film strain gauges on the silicon substrate for silicon-based heterogeneous integration application, IEEE Trans Compon Packaging Manuf Technol 13 (7) (Jul. 2023) 957–964, https://doi.org/10.1109/TCPMT.2023.3297236.

[9] T. Higashi, et al., Physicochemical insights into semiconductor properties of a semitransparent tantalum nitride photoanode for solar water splitting, Phys. Chem. Chem. Phys. 25 (30) (2023) 20737–20748, https://doi.org/10.1039/D3CP02563B.

[10] E. Nurlaela, A. Ziani, K. Takanabe, Tantalum nitride for photocatalytic water splitting: concept and applications, Mater. Renew. Sustain. Energy 5 (4) (Nov. 2016) 18, https://doi.org/10.1007/s40243-016-0083-z.

[11] F.R. Attarzadeh, N. Attarzadeh, S. Vafaeian, A. Fattah-Alhosseini, Effect of pH on the electrochemical behavior of tantalum in borate buffer solutions, J. Mater. Eng. Perform. 25 (10) (Oct. 2016) 4199–4209, https://doi.org/10.1007/s11665-016-2295-x.

[12] A.C. Hee, Y. Zhao, S.S. Jamali, A. Bendavid, P.J. Martin, H. Guo, Characterization of tantalum and tantalum nitride films on Ti6Al4V substrate prepared by filtered cathodic vacuum arc deposition for biomedical applications, Surf. Coat. Technol. 365 (May 2019) 24–32, https://doi.org/10.1016/j.surfcoat.2018.05.007.

[13] J. Corona-Gomez, T.A. Jack, R. Feng, Q. Yang, Wear and corrosion characteristics of nano-crystalline tantalum nitride coatings deposited on CoCrMo alloy for hip joint applications, Mater. Charact. 182 (Dec. 2021) 111516, https://doi.org/10.1016/j.matchar.2021.111516.

[14] R. Li, et al., Tantalum nitride coatings prepared by magnetron sputtering to improve the bioactivity and osteogenic activity for titanium alloy implants, RSC Adv. 7 (87) (2017) 55408–55417, https://doi.org/10.1039/C7RA09032C.

[15] K. Babaei, A. Fattah-alhosseini, H. Elmkhah, O. Imantalab, H. Ghomi, Studying the in vitro corrosion response of nanostructured TaN coatings in Hank's physiological solution, Int. J. Appl. Ceram. Technol. 18 (4) (Jul. 2021) 1269–1280, https://doi.org/10.1111/ijac.13756.
[16] E. Nurlaela, A. Ziani, K. Takanabe, Tantalum nitride for photocatalytic water splitting: concept and applications, Mater. Renew. Sustain. Energy 5 (4) (Dec. 2016) 18, https://doi.org/10.1007/s40243-016-0083-z.
[17] S.K. Kim, B.C. Cha, Deposition of tantalum nitride thin films by D.C. magnetron sputtering, Thin Solid Films 475 (1–2) (Mar. 2005) 202–207, https://doi.org/10.1016/j.tsf.2004.08.059.
[18] M. Grumski, P.P. Dholabhai, J.B. Adams, Ab initio study of the stable phases of 1:1 tantalum nitride, Acta Mater. 61 (10) (Jun. 2013) 3799–3807, https://doi.org/10.1016/j.actamat.2013.03.018.
[19] D. Bernoulli, U. Müller, M. Schwarzenberger, R. Hauert, R. Spolenak, Magnetron sputter deposited tantalum and tantalum nitride thin films: An analysis of phase, hardness and composition, Thin Solid Films 548 (Dec. 2013) 157–161, https://doi.org/10.1016/j.tsf.2013.09.055.
[20] S. Liao, et al., Effect of nitrogen content on the mechanical and biological properties of tantalum nitride coatings, Surf. Coat. Technol. 464 (Jul. 2023) 129544, https://doi.org/10.1016/j.surfcoat.2023.129544.
[21] M. Alperen Polat, et al., Characterization of ta/TaN multi-graded thin film coating synthesized by HiPIMS technique, Materials Open Research 2 (Nov. 2023) 12, https://doi.org/10.12688/materialsopenres.17622.1.
[22] A.H. Ramezani, S. Hoseinzadeh, A. Bahari, The effects of nitrogen on structure, morphology and electrical resistance of tantalum by ion implantation method, J. Inorg. Organomet. Polym. Mater. 28 (3) (May 2018) 847–853, https://doi.org/10.1007/s10904-017-0769-4.
[23] T. Elangovan, et al., Synthesis and high temperature XRD studies of tantalum nitride thin films prepared by reactive pulsed dc magnetron sputtering, J. Alloys Compd. 509 (22) (Jun. 2011) 6400–6407, https://doi.org/10.1016/j.jallcom.2011.03.067.
[24] M. Alishahi, et al., Structural properties and corrosion resistance of tantalum nitride coatings produced by reactive DC magnetron sputtering, RSC Adv. 6 (92) (2016) 89061–89072, https://doi.org/10.1039/C6RA17869C.
[25] W. Lei, et al., Direct synthesis and characterization of single-phase tantalum nitride (Ta2N) nanocrystallites by dc arc discharge, J. Alloys Compd. 459 (1–2) (Jul. 2008) 298–301, https://doi.org/10.1016/j.jallcom.2007.04.219.
[26] X. Zhao, N.P. Magtoto, J.A. Kelber, Chemical vapor deposition of tantalum nitride with tert-butylimino tris(diethylamino) tantalum and atomic hydrogen, Thin Solid Films 478 (1–2) (May 2005) 188–195, https://doi.org/10.1016/j.tsf.2004.10.042.
[27] J.H. Han, et al., Growth of tantalum nitride film as a cu diffusion barrier by plasma-enhanced atomic layer deposition from bis((2-(dimethylamino)ethyl)(methyl) amido)methyl(tert-butylimido)tantalum complex, Appl. Surf. Sci. 362 (Jan. 2016) 176–181, https://doi.org/10.1016/j.apsusc.2015.11.095.
[28] T.H. Kim, G.Y. Yeom, A review of inductively coupled plasma-assisted magnetron sputter system, Appl. Sci. Convergen. Technol. 28 (5) (Sep. 2019) 131–138, https://doi.org/10.5757/ASCT.2019.28.5.131.
[29] S.-I. Baik, Y.-W. Kim, Microstructural evolution of tantalum nitride thin films synthesized by inductively coupled plasma sputtering, Appl. Microsc. 50 (1) (Dec. 2020) 7, https://doi.org/10.1186/s42649-020-00026-7.
[30] A.C. Hee, Y. Zhao, S.S. Jamali, A. Bendavid, P.J. Martin, H. Guo, Characterization of tantalum and tantalum nitride films on Ti6Al4V substrate prepared by filtered cathodic vacuum arc deposition for biomedical applications, Surf. Coat. Technol. 365 (May 2019) 24–32, https://doi.org/10.1016/j.surfcoat.2018.05.007.
[31] Y. Lu, et al., Wideband metamaterial absorbers based on conductive plastic with additive manufacturing technology, ACS Omega 3 (9) (Sep. 2018) 11144–11150, https://doi.org/10.1021/acsomega.8b01223.
[32] C. Chen, et al., Microstructure evolution and mechanical properties of laser additive manufactured Ti6Al4V alloy under nitrogen-argon reactive atmosphere, Mater. Sci. Eng. A 841 (Apr. 2022) 143076, https://doi.org/10.1016/j.msea.2022.143076.
[33] O. Cakmak, S.-H. Lee, S.G. Chung, D.-R. Eo, H. Yeom, J.-W. Cho, In-situ synthesis of nitrides and oxides through controlling reactive gas atmosphere during laser-powder bed fusion of Fe-12Cr-6Al, Mater. Des. 240 (Apr. 2024) 112862, https://doi.org/10.1016/j.matdes.2024.112862.
[34] ASTM International, ASTM B962–23: Standard Test Methods for Density of Compacted or Sintered Powder Metallurgy (PM) Products Using Archimedes' Principle, Sep. 2023.
[35] L. Lutterotti, Total pattern fitting for the combined size–strain–stress–texture determination in thin film diffraction, Nucl. Inst. Methods Phys. Res. B 268 (3–4) (Feb. 2010) 334–340, https://doi.org/10.1016/j.nimb.2009.09.053.
[36] V. Livescu, C.M. Knapp, G.T. Gray, R.M. Martinez, B.M. Morrow, B.G. Ndefru, Additively manufactured tantalum microstructures, Materialia (Oxf) 1 (Sep. 2018) 15–24, https://doi.org/10.1016/j.mtla.2018.06.007.
[37] International Organization for Standardization, ISO 6507-1:2023: Metallic materials - Vickers hardness test - Part 1: Test method, 2023.
[38] International Organization for Standardization, ISO 14577-1:2015: Metallic materials - Instrumented indentation test for hardness and materials parameters - Part 1: Test method, 2015.
[39] H. Ono, K. Koyanagi, Infrared absorption peak due to ta=O bonds in Ta2O5 thin films, Appl. Phys. Lett. 77 (10) (Sep. 2000) 1431–1433, https://doi.org/10.1063/1.1290494.
[40] R. Lide David (Ed.), CRC Handbook of Chemistry and Physics, 85th ed., CRC Press, Boca Raton, FL, 2005.
[41] D. Simson, S.K. Subbu, Effect of process parameters on surface integrity of LPBF Ti6Al4V, Procedia CIRP 108 (2022) 716–721, https://doi.org/10.1016/j.procir.2022.03.111.
[42] A.A.A. Aliyu, et al., Additive manufacturing of tantalum scaffolds: processing, microstructure and process-induced defects, Int. J. Refract. Met. Hard Mater. 112 (Apr. 2023) 106132, https://doi.org/10.1016/j.ijrmhm.2023.106132.
[43] Y.X. Leng, et al., Biomedical properties of tantalum nitride films synthesized by reactive magnetron sputtering, Thin Solid Films 398–399 (Nov. 2001) 471–475, https://doi.org/10.1016/S0040-6090(01)01448-1.